

Proton acceleration in plasma turbulence driven by high-energy lepton jets

Gaowei Zhang(张高维), Zhengming Sheng(盛政明), Suming Weng(翁苏明), Min Chen(陈民), and Jie Zhang(张杰)

Citation: Chin. Phys. B, 2024, 33 (**11**): 115203. DOI: 10.1088/1674-1056/ad7b01
Journal homepage: http://cpb.iphy.ac.cn; http://iopscience.iop.org/cpb

What follows is a list of articles you may be interested in

Effects of plasma radiation on the nonlinear evolution of neo-classical tearing modes in tokamak plasmas with reversed magnetic shear

Shuai Jiang(姜帅), Zheng-Xiong Wang(王正汹), Lai Wei(魏来), and Tong Liu(刘桐)
Chin. Phys. B, 2023, 32 (**10**): 105203. DOI: 10.1088/1674-1056/acedf7

Gyrokinetic simulation of low-*n* Alfvénic modes in tokamak HL-2A plasmas

Wen-Hao Lin(林文浩), Ji-Quan Li(李继全), J Garcia, and S Mazzi
Chin. Phys. B, 2023, 32 (**2**): 025202. DOI: 10.1088/1674-1056/ac6b23

Role of the zonal flow in multi-scale multi-mode turbulence with small-scale shear flow in tokamak plasmas

Hui Li(李慧), Jiquan Li(李继全), Zhengxiong Wang(王正汹), Lai Wei(魏来), and Zhaoqing Hu(胡朝清)
Chin. Phys. B, 2022, 31 (**6**): 065207. DOI: 10.1088/1674-1056/ac6011

A nonlinear wave coupling algorithm and its programing and application in plasma turbulences

Yong Shen(沈勇), Yu-Hang Shen(沈煜航), Jia-Qi Dong(董家齐), Kai-Jun Zhao(赵开君), Zhong-Bing Shi(石中兵), and Ji-Quan Li(李继全)
Chin. Phys. B, 2022, 31 (**6**): 065206. DOI: 10.1088/1674-1056/ac4233

Filamentation instability in two counter-streaming laser plasmas

Hui Liu(刘慧), Quan-Li Dong(董全力), Da-Wei Yuan(袁大伟), Xun Liu(刘勋), Neng Hua(华能), Zhan-Feng Qiao(乔战峰), Bao-Qiang Zhu(朱宝强), Jian-Qiang Zhu(朱健强), Bo-Bin Jiang(蒋柏彬), Kai Du(杜凯), Yong-Jian Tang(唐永健), Gang Zhao(赵刚), Xiao-Hui Yuan(远晓辉), Zheng-Ming Sheng(盛政明), Jie Zhang(张杰)
Chin. Phys. B, 2016, 25 (**12**): 125201. DOI: 10.1088/1674-1056/25/12/125201

RAPID COMMUNICATION

Proton acceleration in plasma turbulence driven by high-energy lepton jets

Gaowei Zhang(张高维)[1,2], Zhengming Sheng(盛政明)[1,2,3,†], Suming Weng(翁苏明)[1,2], Min Chen(陈民)[1,2], and Jie Zhang(张杰)[1,2,3]

[1] *Key Laboratory for Laser Plasmas (MOE), School of Physics and Astronomy, Shanghai Jiao Tong University, Shanghai* 200240, *China*
[2] *Collaborative Innovation Center of IFSA, Shanghai Jiao Tong University, Shanghai* 200240, *China*
[3] *Tsung-Dao Lee Institute, Shanghai Jiao Tong University, Shanghai* 201210, *China*

(Received 15 August 2024; revised manuscript received 9 September 2024; accepted manuscript online 14 September 2024)

The interaction of high energy lepton jets composed of electrons and positrons with background electron–proton plasma is investigated numerically based upon particle-in-cell simulation, focusing on the acceleration processes of background protons due to the development of electromagnetic turbulence. Such interaction may be found in the universe when energetic lepton jets propagate in the interstellar media. When such a jet is injected into the background plasma, the Weibel instability is excited quickly, which leads to the development of plasma turbulence into the nonlinear stage. The turbulent electric and magnetic fields accelerate plasma particles via the Fermi II type acceleration, where the maximum energy of both electrons and protons can be accelerated to much higher than that of the incident jet particles. Because of background plasma acceleration, a collisionless electrostatic shock wave is formed, where some pre-accelerated protons are further accelerated when passing through the shock wave front. Dependence of proton acceleration on the beam-plasma density ratio and beam energy is investigated. For a given background plasma density, the maximum proton energy generally increases both with the density and kinetic energy of the injected jet. Moreover, for a homogeneous background plasma, the proton acceleration via both turbulent fields and collisionless shocks is found to be significant. In the case of an inhomogeneous plasma, the proton acceleration in the plasma turbulence is dominant. Our studies illustrate a scenario where protons from background plasma can be accelerated successively by the turbulent fields and collisionless shocks.

Keywords: Weibel instability, turbulence, collisionless shock, ion acceleration

PACS: 52.35.–g, 52.35.Ra, 52.35.Tc, 52.35.Qz **DOI:** 10.1088/1674-1056/ad7b01

1. Introduction

The origins of high-energy cosmic rays, their generation mechanisms and propagation in the interstellar medium have long been topics of great interest since they were discovered more than a century ago. Key mechanisms for cosmic ray generation include the Fermi acceleration[1,2] and plasma wave acceleration,[3,4] where the former is considered to be responsible for particles with energy up to 10^{19} eV and the latter could lead to even higher energy acceleration.[5–9] The Fermi acceleration is realized either through the diffusive shock acceleration[10–12] (so called the first-order Fermi acceleration) or the reflection from randomly moving magnetic mirrors[13,14] (i.e., the second-order Fermi acceleration). On the other hand, even though the Fermi acceleration provides a global picture of the acceleration mechanisms, it may be initiated through different processes locally. For example, it is believed that the generation of cosmic rays could be related to relativistic celestial jets.[15–17]

Relativistic jets are associated with some of the most violent high-energy astrophysical phenomena in the universe, such as GRB,[18–20] AGN,[21] XRB,[22] and TDE.[23] Relativistic jets are usually assumed to be composed of pure leptons (i.e., electrons and positrons). When such jets propagate in the interstellar medium,[24] micro-instabilities such as the Weibel instability will be driven,[25,26] which can produce strong magnetic fields and subsequently lead to the formation of collisionless shock waves in the interstellar medium. Fermi type of acceleration processes could be triggered. This system is directly related to some astrophysical models, such as the neutron star wind[27] and the fireball model of GRBs.[28] Although both Fermi acceleration and collisionless shock acceleration have been studied in detail in many literatures,[29–31] mostly these two phenomena have been studied separately. For the simulation of collisionless shock waves, one usually takes a configuration in which an incident jet from a boundary is reflected at another boundary to generate a shock wave close to the interface of the incoming and reflection flows. Thus, the plasma and jet parameters applied for the density ratio and distributions are limited. Recently, it was found that a two-stage acceleration process of protons may occur naturally in the interaction of an energetic electron–positron jet with a background electron–proton plasma,[32] where the plasma electrons and protons are accelerated by the turbulent electromagnetic fields first. Later, a collisionless shock wave is

†Corresponding author. E-mail: zmsheng@sjtu.edu.cn

© 2024 Chinese Physical Society and IOP Publishing Ltd

formed in the preheated plasma and some protons are further accelerated by the shock wave.

In this paper, the interaction of lepton jets with background plasma is further investigated numerically by using particle-in-cell (PIC) simulations. Attention is paid to the effects of the energy and density of the lepton jets as well as the background plasma parameters on the acceleration of plasma electrons and protons. The acceleration involves two stages, i.e., the pre-acceleration in turbulent electric and magnetic fields generated via the Weibel-type instability at the early stage and succeeding acceleration in collisionless shocks formed at later stage. It is shown that the maximum energy of plasma electrons and protons can be much higher than the initial particle energy of the lepton jets. The paper is organized as follows. In Section 2, the formation of turbulent fields due to the Weibel-type instability and collisionless shocks is described. The plasma particle acceleration found in these processes is analyzed in Section 3. The effects of lepton jet and plasma parameters on the acceleration are presented in Section 4. The paper is concluded in Section 5.

2. Generation of turbulent fields and collisionless shock waves

To investigate the interaction of a lepton jet with background plasma, we carry out two-dimensional PIC simulations with the code Osiris.[33] We take a simulation box with the dimension of $[-10,900]d_e$ and $[0,95]d_e$ along the x and y directions, respectively, where d_e is the plasma skin depth given by $d_e = c/\omega_p$ with c the vacuum light speed, $\omega_p = 4\pi N_{e0}e^2/m_e$ the electron plasma frequency, N_{e0} the initial plasma density, and m_e the electron mass. Initially, the simulation box is filled with electron–ion plasma uniformly, where the ion–electron mass ratio $m_i/m_e = 1836$ is taken, i.e., the ions are protons with charge number $Z = 1$, and the initial temperature of the background plasma is 20 eV. An electron–positron jet with initial energy of 50.6 MeV (corresponding to the relativistic factor $\gamma = 100$) is incident from the left boundary along the $+x$ direction into the background plasma. The ratio of the initial lepton jet density n_{b0} and the initial background plasma density N_{p0} to the beam density is $\alpha = n_{b0}/N_{p0} = 1$. The simulation box is divided into 20 grids per d_e in the x direction and 10 grids per d_e in the y direction. Each grid has 4 macroparticles of each particle type. The time step of the simulation is $0.04/\omega_p$. We take open boundary conditions in the x direction and periodic boundary conditions in the y direction. The incident lepton jet is initially uniform in the y direction and is semi-infinite along the x direction.

As shown in Figs. 1(a) and 1(b), the Weibel instability develops strongly after a few hundreds of $1/\omega_p$, producing distinct filamentary structures[34] in $x < 100d_e$. Initially, these filamentary structures have diameters about a few d_e, close to

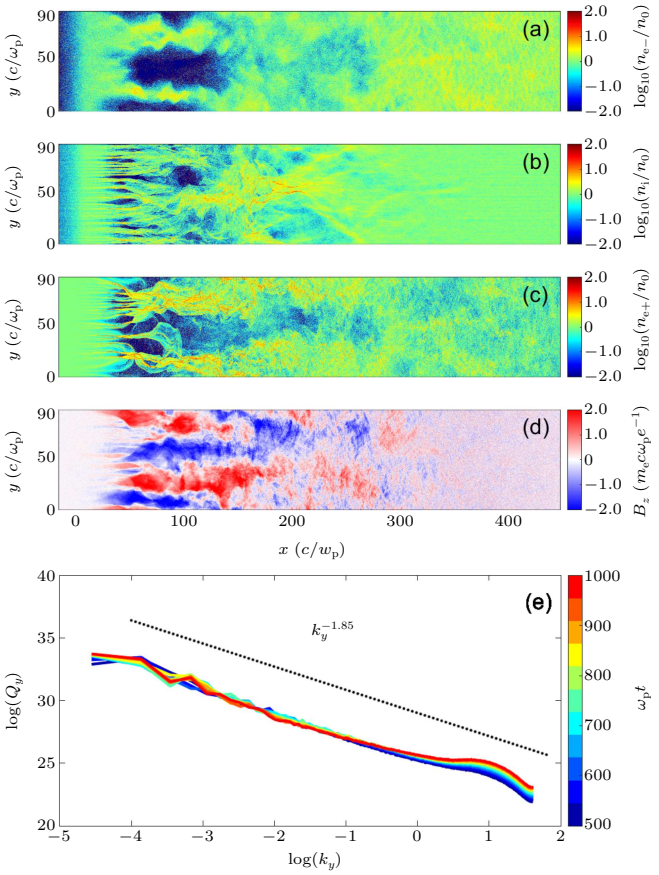


Fig. 1. Snapshots of the spatial distributions of the background plasma electron density (a), background plasma ion density (b), injected positrons (c), and the magnetic fields (d) at $t = 500\omega_p^{-1}$. (e) Fourier spectrum of magnetic fields distributed between [0,400] d_e within the time window 500–1000 ω_p^{-1} represented by color lines, where the black dashed line shows the power-law slope of $k_y^{-1.85}$.

the theoretical values for Weibel filaments. Later, these filamentary energetic beams penetrate deeper into the background plasma and coalesce to form larger filamentary structures, creating a highly turbulent region between $x = [100,400]d_e$, as shown in Figs. 1(a) and 1(c). In this turbulent region, the density of ions in the background plasma can vary by up to three orders of magnitude within a few tens of d_e, as shown in Fig. 1(a). Such violent turbulence can produce very strong magnetic fields,[35–39] as shown in Fig. 1(d). As the lepton flow continues to propagate in plasma, the turbulent fields are still excited in the region $x > 300d_e$, but they appear at a relatively low level. This reduced turbulent magnetic field generation could be associated with the plasma heating and the buildup of a high transverse temperature of the jet, as discussed in the following. We have analyzed the spectrum of the magnetic fields along the y-direction by integrating the spectrum along this direction

$$Q_y = \int |\tilde{B}_z(k_x,k_y)|^2 \,\mathrm{d}k_y,$$

where $\tilde{B}_z(k_x,k_y)$ is the Fourier transform of $B_z(x,y)$ with k_x and k_y normalized by ω_p/c. It is found that the turbulent magnetic fields have a power law spectrum with an index of about -1.8,

which is close to the theoretical value of electron magnetohydrodynamic turbulence[40,41] estimated to $-5/3$ for $k \ll 1$ and $-7/3$ for $k \gg 1$.

The reduction of plasma turbulence in the region $x > 300d_e$ suggests that the Weibel instability is developed weakly in that region. This is associated with the development of the transverse beam temperature of the injected lepton flow, which tends to suppress the development of the Weibel instability.[42–45] As shown in Fig. 2 for the distributions of the longitudinal and transverse momenta for the injected positron beam, the average longitudinal momentum is reduced generally and high transverse momentum is built up quickly due to the development of the turbulent fields at the early stage. This explains why the Weibel instability is only weakly developed at late stage.

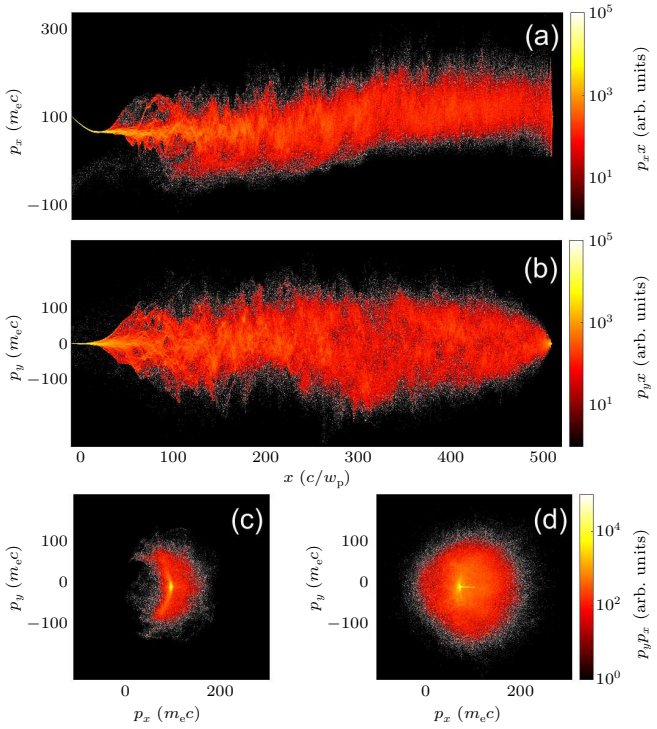


Fig. 2. Panels (a) and (b) show respectively the distributions of longitudinal and transverse momenta of positrons along the x-direction at $t = 500\omega_p^{-1}$. Panels (c) and (d) show the phase space distributions of position momenta at $t = 200\omega_p^{-1}$ and $500\omega_p^{-1}$, respectively.

Even though the turbulent fields decay along the propagation direction, it is found that a collisionless shock wave starts to build up in the region behind $400d_e$. As shown in Fig. 3(a), a local high magnetic field region together with a local high electric field region propagates at a speed of about $0.24c$, which is associated with the collisionless shock wave.[46–48] Figure 3(b) shows a snapshot of the longitudinal intensity distributions of electric and magnetic fields at $T = 2000\omega_p^{-1}$. These fields near the shock front at $x \sim 600d_e$ are relatively high. Associated with the shock formation are the longitudinal distributions of the background plasma proton density and the injected positron density. A sharp proton density front is built up at $x = 500d_e$ at the time $T = 1500\omega_p^{-1}$ and moves to near $x = 600d_e$ at the time $T = 2000\omega_p^{-1}$ as shown in Fig. 3(c), which is associated the formation of the collisionless shock. In the region of $0 < x < 300d_e$, the positron density is packed up to $n_{e0+}/n_{b0} = 2$, while most of the background ions are blown away. In the region of $200d_e < x < 600d_e$ behind the shock front, where the turbulent magnetic field strength is low, the total density of background plasma ions and positrons forms a plateau with the density $(N_i + n_{e0+})/N_{p0} \sim 3$. This appears to be comparable to a hydrodynamic shock with the density jump at the shock front given by $N_{p1}/N_{p2} = (\gamma_{ad}\gamma_{sh} + 1)/(\gamma_{ad} - 1) \sim 3$ with the adiabatic coefficient $\gamma_{ad} = 2$ in the two-dimensional geometry and $\gamma_{sh} = (1 - v_s^2/c^2)^{-1/2}$.

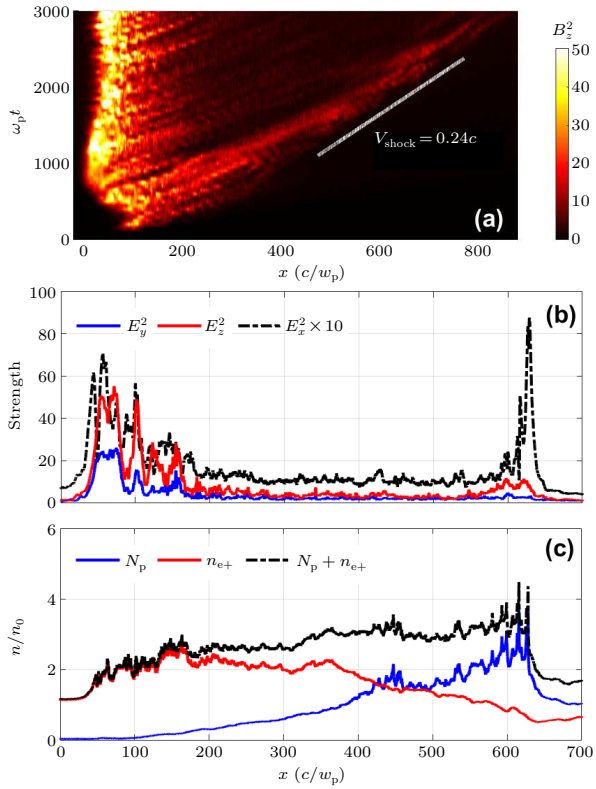


Fig. 3. (a) The distribution of the magnetic field energy in time and space along the x-direction after averaging along the y direction. The white dashed line indicates the shock wave propagation speed of $0.24c$. (b) Longitudinal distributions of energy of electric fields E_x and E_y, and magnetic field B_z at $T = 2000\omega_p^{-1}$ obtained after averaging along the y-direction. Strength indicates E_x^2, E_y^2, and B_z^2, where the fields are all normalized by $m_e\omega_p c/e$. (c) Longitudinal distributions of background ions and injected positrons at $T = 2000\omega_p^{-1}$ obtained after averaging along the y-direction. The densities are normalized by their initial densities N_{p0} and n_{b0}.

3. Acceleration of background electrons and protons

As shown above, the turbulent electric and magnetic fields as well as collisionless shocks[49] are formed at different stages. Figure 4(a) shows a snapshot of the magnetic field distribution at $T = 2000\omega_p^{-1}$. Associated with turbulent field excitation and collisionless shock formation, background electrons and ions are accelerated both longitudinally and trans-

versely, as shown in Figs. 4(b) and 4(c) for the background ions. It is shown that the transverse acceleration along the y direction is symmetric, while the longitudinal acceleration is mainly in the forward direction. The transverse and longitudinal accelerations in the region $x < 600d_e$ behind the shock are due to the turbulent field excitation. At the shock front, some ions in front of the shock are trapped and accelerated by the shock wave, where they gain a speed at twice the shock speed. As the shock speed is about $v_s = 0.24c$ according to Fig. 3(a), the trapped ion speed should be near $0.48c$ as shown in Fig. 4(b).

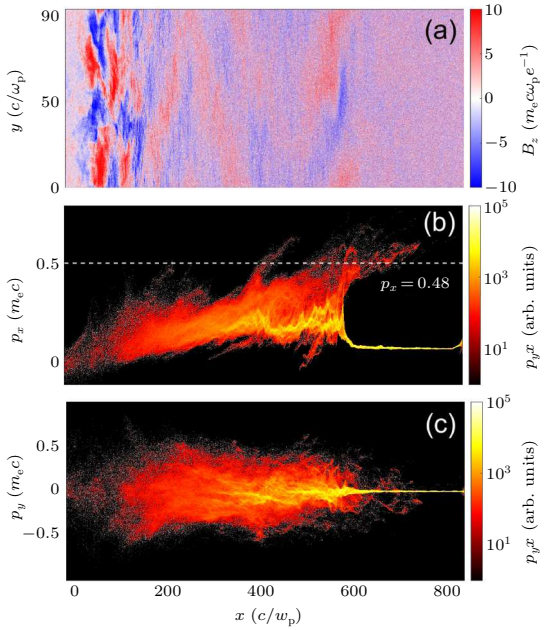


Fig. 4. (a) Spatial distribution of the turbulent magnetic field at $T = 2000\omega_p^{-1}$. Panels (b) and (c) show respectively the phase space distributions of the longitudinal and transverse momenta of the background plasma ions at $T = 2000\omega_p^{-1}$.

We have also traced the phase-space trajectories of selected particles accelerated in the two stages as shown in Fig. 5. Figures 5(a), 5(c), and 5(d) show that a group of ions are accelerated in the first stage by the turbulent magnetic field[50] excited by the Weibel instability, gaining energy both in the x and y directions until about $t = 800\omega_p^{-1}$. When the ions move to the range of $300d_e < x < 500d_e$, they encounter the turbulent electric and magnetic fields downstream of the shock wave and obtain the second acceleration. At this time, the velocity of some ions in the y direction is completely reversed, and the momentum in the x direction is further increased. The ions pass through the shock wave front at $t = 1200\omega_p^{-1}$, and obtain the third acceleration. The three stages of acceleration marked with I, II, and III are shown in Fig. 5(c). Figures 5(b), 5(e), and 5(f) show two groups of accelerated ions, which are originally located in the regions with low turbulent fields excited. They are first weakly accelerated by the turbulent magnetic fields and then significantly accelerated by the collisionless shock.

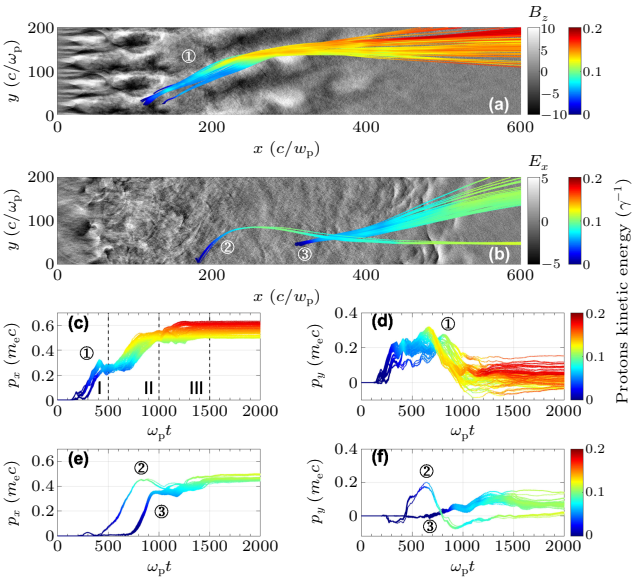


Fig. 5. Trajectories of selected ions accelerated in the turbulent fields and shock waves and their momentum change with time. (a) Trajectories of 100 selected ions with the large transverse momentum accelerated at the early stage up to $T = 900\omega_p^{-1}$, which are marked as group 1. (b) Trajectories of 100 selected ions accelerated dominantly by the longitudinal electric fields near the shock front at the late stage up to $T = 1500\omega_p^{-1}$, which are marked as groups 2 and 3. Panels (c) and (d) show the evolution of longitudinal and transverse momenta for ions from group 1. Panels (e) and (f) show the evolution of longitudinal and transverse momenta for ions from groups 2 and 3. The color bars correspond to the ion energy.

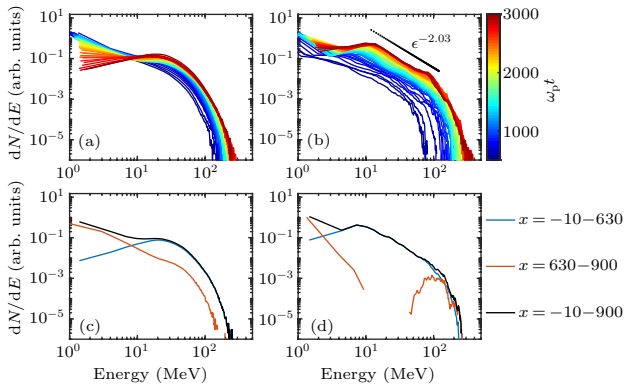


Fig. 6. Panels (a) and (b) show respectively the evolution of the electron energy spectra and ion energy spectra obtained at different time between $[500, 3000]\omega_p^{-1}$. Panels (c) and (d) show respectively the energy spectra for electrons and ions obtained at $T = 2000\omega_p^{-1}$ from the whole plasma and for those located near the collisionless shock front.

The spectra of accelerated background electrons and ions are shown in Fig. 6. Generally, both electrons and ions have thermal energy spectra,[51] where the maximum energies of electrons are accelerated to about 300 MeV and ions are accelerated to above 400 MeV at $T = 3000\omega_p^{-1}$. These are much higher than the injected lepton flow at 50 MeV. The electron energy spectrum appears to have two temperatures, which is similar to that found by other researchers.[2] In some energy range below 100 MeV, the ion spectrum has a power-law distribution $\sim \varepsilon^{-2}$, as shown in Fig. 6(b), which is typical for the type of Fermi acceleration. Before the formation of the collisionless shock at $x \sim 500c/\omega_p$ around $T = 1500/\omega_p$, the maximum energy for both electrons and protons is already above

200 MeV. At later time with the formation of the collisionless shock, some ions are trapped and accelerated further by the shock. For protons trapped and accelerated by the shock, the proton speed shall be larger than $2v_s$, corresponding to the proton energy of about 117 MeV for $v_s = 0.24c$. Therefore, for protons with higher energy, significant part of their energy is contributed by the turbulent field acceleration. Note that the shock formation is associated with the electron temperature. This temperature can be estimated by the average energy of the background electrons, which is found to be about 14 MeV according to the simulation. The corresponding ion acoustic speed is about $c_s = (\gamma_{ad} T_{pe}/m_i) = 0.13c$, where $\gamma_{ad} = 2$ is the adiabatic coefficient in a two-dimensional system. Thus, the Mach number for the collisionless shock in the present simulation is $M = 1.9$.

4. Effects of jet and plasma parameters on acceleration

4.1. Effect of the density ratio between jet and plasma

As the generation of turbulent fields and shock waves depends significantly on parameters of the lepton jet and the background plasma, it is expected that these parameters can have significant effects on the resulting acceleration of background plasma acceleration. We first consider the effect of the density ratio between the incident lepton jet and the background plasma. Figures 7(a) and 7(b) show the energy spectra of electrons and ions from the background plasma. As the jet density increases, the energy of background electrons and ions increases significantly. This is because the increase of the jet density enhances the growth rate of the Weibel instability and the intensity of turbulent magnetic fields, which naturally enable the plasma electrons and ions to gain higher energy from the turbulent fields. At the same time, the increase of the turbulent fields not only enhances the particle acceleration, but also enables the shock wave to form at earlier time with a higher shock speed. As shown in Figs. 7(c) and 7(d), the speed of the shock wave increases monotonically with the lepton jet density. Thus, the proton energy gain from the shock wave acceleration also becomes more effective with increasing jet density. On the other hand, when the density ratio is too high, such as $\alpha = 10$, no collisionless shock is formed clearly within the limited simulation time up to $T = 2000\omega_p^{-1}$ and simulation box, even though background plasma electrons and ions are accelerated to higher energy. The acceleration is mainly contributed by the turbulent fields excited in a larger area in this case.

4.2. Effect of the lepton jet energy

For a given density ratio between the lepton jet and the background plasma density, the energy of background plasma electrons and ions depends upon the different γ values of the incident lepton jet, as shown in Fig. 8. For example, when $\gamma = 300$, the cutoff energy of both electrons and protons reaches above 500 MeV. The speed of the shock wave also increases obviously with γ as shown in Figs. 8(c) and 8(d). When γ increases from 50 to 300, the shock speed increases from 0.19 to 0.35. Note that the cutoff energy is much higher than that expected from the shock acceleration as a significant part of the proton energy is contributed by the turbulent field acceleration as mentioned above. Figure 8(c) shows that the shock front is relatively steeper with a smaller γ due to the fact that more background protons are accelerated. In the meanwhile, the higher energy of the lepton jet allows the Weibel instability and turbulent fields to be excited in a wider space. This also helps to enhance the acceleration of background plasma particles by the turbulent fields.

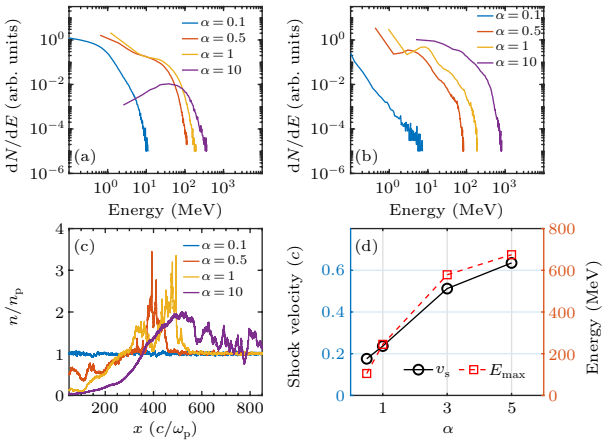


Fig. 7. Effects of the density ratio between the lepton jet and background plasma on plasma acceleration, where the results are shown for the lepton jet with $\gamma = 100$ at $T = 2000\omega_p^{-1}$. (a) Electron energy spectrum, (b) proton energy spectrum, (c) proton density distributions along the x-direction averaged over the y-direction, (d) shock velocity and the cutoff energy of protons for different density ratio $\alpha = n_{b0}/N_{p0}$.

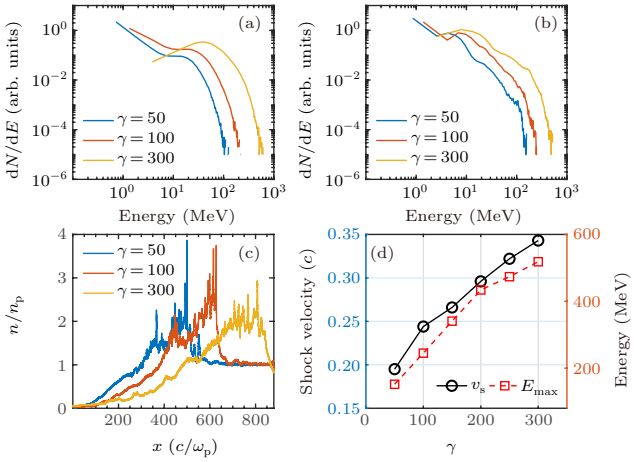


Fig. 8. Effects of the lepton jet energy on plasma acceleration under the density ratio $\alpha = n_{b0}/N_{p0} = 1$ at $T = 2000\omega_p^{-1}$. (a) Electron energy spectra, (b) proton energy spectra, (c) proton density distributions along the x-direction averaged over the y-direction, (d) shock wave velocity and ion energy spectrum cutoff energy for different γ of the incident lepton jet.

4.3. Effects of nonuniform background plasma density

In previous studies, we have assumed that the background plasma density is uniform. Generally, there may be some density nonuniformity. In order to analyze the effects of inhomogeneous density plasma, we compare three cases: (a) plasma with a positive density gradient, where the density rises linearly with α changing from 0.5 to 1 within $0 < x < 900d_e$; (b) plasma with a uniform density distribution for $0 < x < 900d_e$; (c) plasma with a negative density gradient, where the density falls linearly with α changing from 1 to 0.5 within $0 < x < 900d_e$. Figures 9(a1), 9(b1) and 9(c1) compare the evolution of the background ion density with time for the three cases. In case (a), it is found that the shock wave forms later when the background plasma density rises gradually, and the lower density at the beginning is beneficial to the transmission of lepton jet, expanding the region dominated by the Weibel instability, thus accelerating the background ions randomly to higher energy. In case (c), it is found that the collisionless shock wave is not formed clearly. In uniform plasma, the shock wave is formed in a large area. These are in agreement with the formation of longitudinal electric field distributions shown in Figs. 9(a3), 9(b3), and 9(c3) for the three cases. Associated with the shock formation, high magnetic fields are also formed near the shock front as shown in Figs. 9(a2), 9(b2), and 9(c2). One notes that even though there is no shock formation in case (c), a localized high magnetic field region is also found. It propagates with a faster speed than the shock wave found in case (b), and thus cannot trap enough background protons and lead to shock formation.

Corresponding to the field distributions shown above, the energy distributions for accelerated background plasma electrons and protons are also different as shown in Fig. 10. It appears that electrons can be accelerated to higher energy in inhomogeneous plasma than in homogeneous plasma, in particular when the plasma density has a positive density gradient, as shown in Figs. 10(a1), 10(b1), and 10(c1). In this case, a larger area of plasma turbulent field is found as shown in Fig. 9(a2). This enables the electrons to be accelerated to higher energy. Similarly, background ions are also accelerated to higher energy in plasma with a positive density gradient, as shown in Figs. 10(a2), 10(b2), and 10(c2). In the case with a decreasing density profile, the maximum ion energy is also higher than that found for homogeneous plasma. In this case, it is found that strong turbulent fields are also driven in a large area as shown in Fig. 9(c2), even though collisionless shock is not formed there. Therefore, the formation of strong turbulent fields in a larger area is found in inhomogeneous plasma in the given conditions, which is responsible for the higher energy of accelerated background electrons and ions.

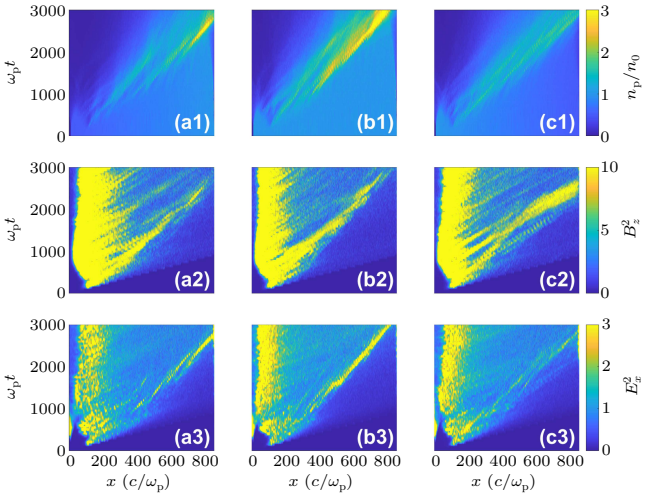


Fig. 9. Spatio-temporal evolution of the background proton density distribution, B_z^2, and E_x^2 under three initial density distributions, i.e., linearly increasing density, uniform density, and linearly decreasing density. (a1), (b1), and (c1) the proton density for the three cases, respectively; (a2), (b2), and (c2) B_z^2 for the three cases, respectively; and (a3), (b3), and (c3) E_x^2 for the three cases, respectively.

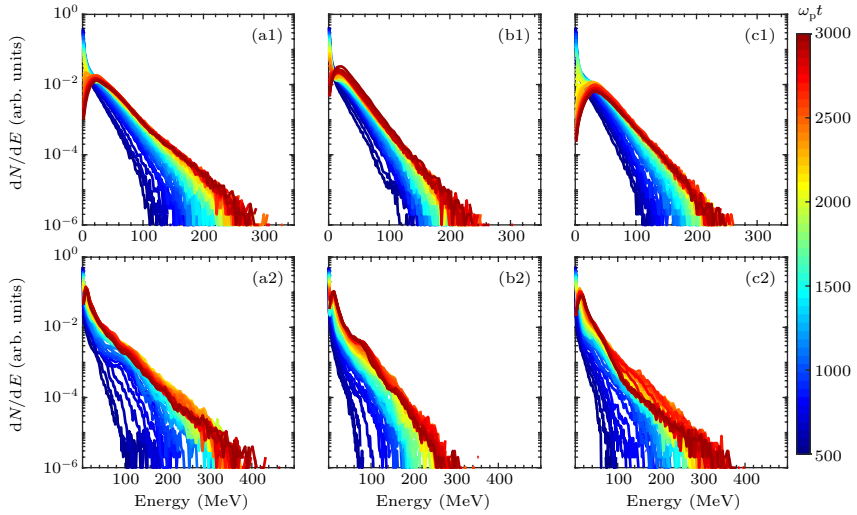


Fig. 10. Panels (a1), (b1), (c1) show background electron energy spectra obtained in plasma with an increasing density profile, a uniform distribution, and a decreasing density profile, respectively, as in Fig. 9. Panels (a2), (b2), (c2) show background ion energy spectra obtained in plasma with an increasing density profile, a uniform distribution, and a decreasing density profile, respectively.

5. Conclusion

In summary, we have carried out numerical simulation studies on the interaction of a lepton jet composed of electrons and positrons with a background plasma composed of electrons and protons. This is similar to the scenario when a lepton jet propagates in the interstellar medium. It is found that the Weibel instability will develop quickly at the beginning, which leads to the formation of strong turbulent fields in plasma. On one hand, the turbulent fields lead to the acceleration of some background electrons and ions to high energy even beyond the initial energy of the lepton jet particles. On the other hand, the turbulent fields tend to thermalize the lepton jet efficiently, so that large transverse momenta of the lepton jet particles are built up. This in turn prevents the excitation of the Weibel instability in large areas along the lepton jet propagation direction. Instead of turbulent field excitation, it is found that collisionless shocks are formed later, which can trap and further accelerate the pre-accelerated protons to higher energies at the shock front. It is noted that the accelerated background electrons show a quasi-thermal distribution for the high energy part, even though the accelerated protons show a power-law spectrum in some energy range.

The relations of the acceleration processes with the density ratio between the lepton jet and the background plasma, the lepton jet energy, and the density distributions are also investigated. A higher jet density tends to increase the excitation of turbulent fields and shock speeds, and thus leads to the energy increase of accelerated background electrons and ions. For a given density ratio, it is found that a higher jet energy can lead to the acceleration of background electrons and ions to higher energy. This is attributed both to a larger space area of the excited turbulent fields and a higher shock speed. Moreover, it is found that inhomogeneous plasma may lead to the acceleration of background electrons and ions to higher energy than that found in homogeneous plasma. This is also attributed to the extended space of the excited turbulent fields in inhomogeneous plasma. Our studies illustrate a scenario where both types of Fermi acceleration may occur during the propagation of a lepton jet in the interstellar medium.

For potential experimental validation, collimated electron–positron pair beams can now be produced with relatively high density via the Trident and Bethe–Heitler process in high Z targets by use of high power lasers.[52,53] On the other hand, it is necessary to ensure that the time duration and size of the electron–positron pair beam exceed the spatiotemporal scale of the Weibel instability. This may require high power lasers at the 10 PW class level, so that lepton jets with enough charge and density could be generated.

Acknowledgments

Project supported by the National Natural Science Foundation of China (Grant Nos. 12135009, 11991074, 11975154, and 12005287). The simulations were performed on the π2.0 supercomputer at the Center for High Performance Computing in Shanghai Jiao Tong University.

References

[1] Fermi E 1949 *Phys. Rev.* **75** 1169
[2] Spitkovsky A 2008 *Astrophys. J.* **682** L5
[3] Ebisuzaki T and Tajima T 2014 *Astropart. Phys.* **56** 9
[4] Tajima T, Yan X and Ebisuzaki T 2020 *Rev. Mod. Plasma Phys.* **4** 7
[5] Bhattacharjee P and Sigl G 2000 *Phys. Rep.* **327** 109
[6] Olinto A 2000 *Phys. Rep.* **333–334** 329
[7] Hinton J 2009 *New J. Phys.* **11** 055005
[8] Sinnis G 2009 *New J. Phys.* **11** 055007
[9] Sommers P and Westerhoff S 2009 *New J. Phys.* **11** 055004
[10] Bell A 1978 *Mon. Not. Royal Astronom. Soc.* **182** 147
[11] Axford W, Leer E and Skadron G 1977 *International Cosmic Ray Conference* vol 11 (Springer)
[12] Blandford R D and Ostriker J P 1978 *Astrophys. J.* **221** L29
[13] Rieger F M, Bosch-Ramon V and Duffy P 2007 *The Multi-Messenger Approach to High-Energy Gamma-Ray Sources* (Springer) pp. 119–125
[14] Gombosi T, Lorencz K and Jokipii J 1989 *J. Geophys. Res. Space Phys.* **94** 15011
[15] Foschini L 2011 arXiv:1105.0772
[16] Lyutikov M, Pariev V I and Gabuzda D C 2005 *Mon. Not. Royal Astronom. Soc.* **360** 869
[17] Zhang J, Sun X N, Liang E W, Lu R J, Lu Y and Zhang S N 2014 *Astrophys. J.* **788** 104
[18] Pruet J, Abazajian K and Fuller G M 2001 *Phys. Rev. D* **64** 063002
[19] Zhang B and Meszaros P 2004 *Internat. J. Mod. Phys. A* **19** 2385
[20] Piran T 2004 *Rev. Mod. Phys.* **76** 1143
[21] Peterson B M 1997 *An Introduction to Active Galactic Nuclei* (Cambridge University Press)
[22] Reig P 2011 *Astrophys. Space Sci.* **332** 1
[23] Gezari S 2021 *Ann. Rev. Astron. Astrophys.* **59** 21
[24] Dyson J E and Williams D A 2020 *The Physics of the Interstellar Medium* (CRC Press)
[25] Weibel E S 1959 *Phys. Rev. Lett.* **2** 83
[26] Fried B D 1959 *The Phys. Fluids* **2** 337
[27] Thompson T A, Burrows A and Meyer B S 2001 *Astrophys. J.* **562** 887
[28] Piran T 1999 *Phys. Rep.* **314** 575
[29] Park H S, Huntington C, Fiuza F, Drake R, Froula D, Gregori G, Koenig M, Kugland N, Kuranz C, Lamb D, *et al.* 2015 *Phys. Plasmas* **22**
[30] Fiuza F, Swadling G, Grassi A, Rinderknecht H, Higginson D, Ryutov D, Bruulsema C, Drake R, Funk S, Glenzer S, *et al.* 2020 *Nat. Phys.* **16** 916
[31] Huang J, Weng S M, Wang X, Zhong J Y, Zhu X L, Li X F, Chen M, Murakami M and Sheng Z M 2022 *Astrophys. J.* **931** 36
[32] Cui Y, Sheng Z, Lu Q, Li Y and Zhang J 2015 *Sci. China Phys. Mechan. Astron.* **58** 105201
[33] Fonseca R A, Silva L O, Tsung F S, Decyk V K, Lu W, Ren C, Mori W B, Deng S, Lee S, Katsouleas T, *et al.* 2002 *Computational Science-ICCS 2002: International Conference Amsterdam, The Netherlands, April 21–24, 2002 Proceedings, Part III 2* (Springer) pp. 342–351
[34] Liu H, Dong Q L, Yuan D W, Liu X, Hua N, Qiao Z F, Zhu B Q, Zhu J Q, Jiang B B, Du K, *et al.* 2016 *Chin. Phys. B* **25** 125201
[35] Bohdan A, Pohl M, Niemiec J, Morris P J, Matsumoto Y, Amano T, Hoshino M and Sulaiman A 2021 *Phys. Rev. Lett.* **126** 095101
[36] Bell A 2004 *Mon. Not. Royal Astronom. Soc.* **353** 550
[37] Peterson J R, Glenzer S and Fiuza F 2021 *Phys. Rev. Lett.* **126** 215101
[38] Peterson J R, Glenzer S and Fiuza F 2022 *Astrophys. J. Lett.* **924** L12
[39] Liu P, Wu D, Hu T, Yuan D, Zhao G, Sheng Z, He X and Zhang J 2024 *Phys. Rev. Lett.* **132** 155103
[40] Biskamp D, Schwarz E and Drake J 1996 *Phys. Rev. Lett.* **76** 1264

[41] Mondal S, Narayanan V, Ding W J, Lad A D, Hao B, Ahmad S, Wang W M, Sheng Z M, Sengupta S, Kaw P, *et al.* 2012 *Proc. Nat. Acad. Sci. USA* **109** 8011
[42] Bret A, Firpo M C and Deutsch C 2005 *Phys. Rev. E* **72** 016403
[43] Silva L O, Fonseca R A, Tonge J W, Mori W B and Dawson J M 2002 *Phys. Plasmas* **9** 2458
[44] Hao B, Ding W J, Sheng Z M, Ren C and Zhang J 2009 *Phys. Rev. E* **80** 066402
[45] Cai H B, Zhu S P, Zheng C Y, He X T and Li J W 2006 *Chin. Phys. Lett.* **23** 161
[46] Forslund D and Freidberg J 1971 *Phys. Rev. Lett.* **27** 1189
[47] Silva L O, Marti M, Davies J R, Fonseca R A, Ren C, Tsung F S and Mori W B 2004 *Phys. Rev. Lett.* **92** 015002
[48] Lemoine M, Gremillet L, Pelletier G and Vanthieghem A 2019 *Phys. Rev. Lett.* **123** 035101
[49] Yuan D W and Li Y T 2015 *Chin. Phys. B* **24** 015204
[50] Yuan D, Lei Z, Wei H, Zhang Z, Zhong J, Li Y, Ping Y, Zhang Y, Li Y, Wang F, *et al.* 2024 *Nat. Commun.* **15** 5897
[51] Zhang Q, Ping Y, An W, Sun W and Zhong J 2022 *Chin. Phys. B* **31** 065203
[52] Sarri G, Poder K, Cole J, Schumaker W, Di Piazza A, Reville B, Dzelzainis T, Doria D, Gizzi L, Grittani G, *et al.* 2015 *Nat. Commun.* **6** 6747
[53] Jiao J, Zhang B, Yu J, Zhang Z, Yan Y, He S, Deng Z, Teng J, Hong W and Gu Y 2017 *Laser and Particle Beams* **35** 234